Shock Response and Phase Transitions of MgO at Planetary Impact Conditions

Seth Root, Luke Shulenburger, Raymond W. Lemke, Daniel H. Dolan, Thomas R. Mattsson, and Michael P. Desjarlais

Phys. Rev. Lett. **115**, 198501 — Published 4 November 2015

DOI: 10.1103/PhysRevLett.115.198501

Shock Response and Phase Transitions of MgO at Planetary Impact Conditions

Seth Root,* Luke Shulenburger, Raymond W. Lemke,
Daniel H. Dolan, Thomas R. Mattsson, and Michael P. Desjarlais
Sandia National Laboratories, Albuquerque, New Mexico 87185, USA
(Dated: October 2, 2015)

The moon-forming impact and the subsequent evolution of the proto-Earth is strongly dependent on the properties of materials at the extreme conditions generated by this violent collision. We examine the high pressure behavior of MgO, one of the dominant constituents in the earth's mantle, using high-precision, plate impact shock compression experiments performed on Sandia National Laboratories' Z-Machine and extensive quantum simulations using Density Functional Theory (DFT) and quantum Monte Carlo (QMC). The combined data span from ambient conditions to 1.2 TPa and 42,000 K, showing solid-solid and solid-liquid phase boundaries. Furthermore our results indicate that under impact the solid and liquid phases coexist for more than 100 GPa, pushing complete melting to pressures in excess of 600 GPa. The high pressure required for complete shock melting has implications for a broad range of planetary collision events.

PACS numbers: 91.60.Hg, 91.60.-x, 81.40.Vw, 71.15.Pd

The leading theory of moon formation is a giant impact event occurring approximately 4.5 billion years ago [1–3]. Complicating the giant impact theory, however, is that the Earth and Moon have a nearly identical chemical and isotopic composition [4]. This implies either the impactor was compositionally similar to the proto-Earth [5] or extensive mixing of the post impact materials occurred. Post impact mixing for chemical equilibration in the proto-Lunar disk has been shown in simulations [6], but requires melting and vaporization of the mantle in order for material to diffuse. Other impact events, such as the formation of chondrules from impact jetting [7], depend on the melting of material during collisions. The simulations needed to test these planetary collisions require an accurate understanding of mantle materials at extreme pressures and temperatures. Unfortunately, the phase diagram and melt line of the most common mantle materials is not well constrained at these conditions [8].

Advanced facilities for performing dynamic compression experiments have greatly increased the pressure and temperature regimes that can be probed for important planetary materials [9–12]. The ability to perform experiments with steady planar shocks and with well-characterized impactors and targets is critical for determining the equation of state (EOS) and the phase. To fully address the physics relevant to planetary science, this thermodynamic information must be augmented with an understanding of the phase transformations.

In this work we focus on MgO, the end-member of the MgO-FeO solid solution series, a major constituent of the earth's mantle [13] and likely other terrestrial planets [14, 15] including exoplanets[16]. At ambient conditions, MgO exists in a NaCl (B1) lattice structure, which is stable over a wide pressure-temperature range [17–20]. Dynamic compression experiments starting from ambient temperature single crystals [21–25], from polycrystalline samples [26, 27], and from T_0=1850 K and 2300 K [28] show no indications of phase transitions up to 230 GPa. Most *ab initio* studies of the phase diagram show three phases: the B1 solid, the B2 (CsCl) solid, and the liquid [29–31], but disagree on the location of the boundaries. Along the Hugoniot, which is relevant for planetary impact scenarios, the locations of the B1-B2 and melt transitions have not been precisely determined.

Recently McWilliams *et al.* showed that MgO can be dynamically compressed to pressures >1 TPa using a decaying shock technique [32]. The authors proposed locations for the B1-B2 and B2-liquid transitions along the Hugoniot, but the measurements relied heavily on an extrapolation of prior MgO Hugoniot data, which was not well known above 230 GPa. Additionally, they claim the Hugoniot quickly crosses the coexistence region between B2 and liquid, but has a large coexistence region between B1-B2 solid. Consequently, they infer the unlikely scenario that the B1-B2 transition has a larger entropy change than the B2-liquid transition contrary to earlier DFT studies [17, 31]. Thus, further examination of the shock response of MgO is required.

We present a comprehensive study of the MgO Hugoniot using experiments, density functional theory (DFT), and quantum Monte Carlo (QMC) methods over a wide pressure range covering the B1, the B2, and the liquid phases from 0.27 to 1.2 TPa. The high-precision data constrain the Hugoniot at multi-Mbar pressures, and the DFT and QMC results further elucidate information on the phase boundaries, finding a relatively large volume collapse on the B1 to B2 transition and a melting transition primarily driven by an increase in entropy. This work provides accurate EOS data at extreme conditions and furthermore reveals lower limits of the relative impact velocity required to melt MgO in an impact scenario.

To attain planetary impact conditions, we performed a series of shock compression experiments using the Sandia Z-Machine [33]. The Z-machine is a pulsed power system

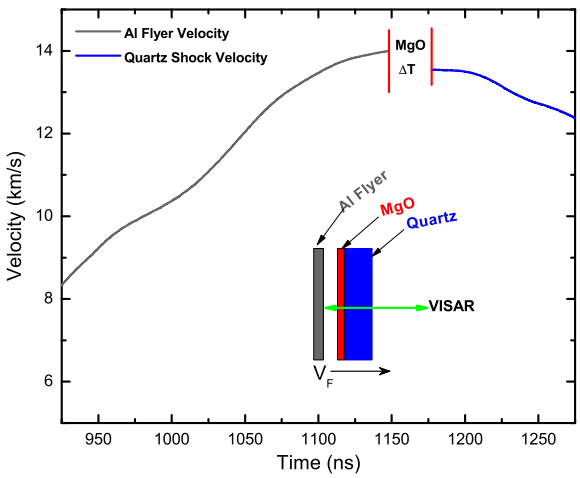

FIG. 1. The experimental configuration and representative VISAR data. The VISAR measures the Al flyer velocity (V_F, grey line) as it approaches the MgO. For this low velocity impact, the VISAR loses signal upon impact with the MgO. As the shock transits into the quartz, the VISAR signal returns and the quartz shock velocity is measured (blue line).

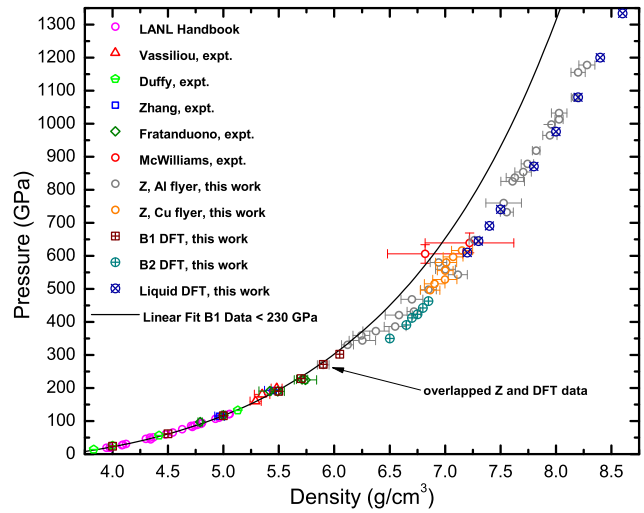

FIG. 2. The MgO Hugoniot data in $\rho - P$ space from Z experiments, previous experimental data[21–25, 32], and our DFT results. The Z data deviate from the extrapolation of the fit to the B1 data from < 230 GPa suggesting the location of the B1-B2 phase transition

capable of producing shaped current pulses and induced magnetic fields in excess of 20 MA and 10 MG respectively. The combined current and magnetic field densities generate magnetic pressures up to 650 GPa that can accelerate aluminum flyers up to 40 km/s [34].

Figure 1 shows a schematic view of the target geometry; a more detailed Z target geometry is found elsewhere [35]. An Al flyer plate is shocklessly accelerated toward the target stack consisting of a single-crystal MgO sample ([100], 300-500 μm, Asphera Corp., $\rho_0 = 3.584$ g/cm^3) and quartz window. For some experiments, a Cu flyer was used. Although the back side of the flyer is melted by the high current, the impact side of the flyer remains solid density at impact [34]. A velocity interferometer system for any reflector (VISAR) measures the flyer plate velocity (V_F) up to impact at the target (Fig. 1). Impact produces a steady shock in the MgO sample. At low impact velocities and consequently, low shock pressures, the MgO sample scatters light from the VISAR preventing direct measurement of the shock velocity. Instead, fiducials are observed in the VISAR signal (see supplemental [36]) that correspond to impact and to shock transit into the quartz window. In this case, we calculated the MgO shock velocity (U_S) using the transit time determined from the fiducials and the measured thickness. At high impact velocities, the shock front is reflective and the VISAR directly measures the MgO shock velocity. Multiple VISAR signals [36] were recorded for each sample eliminating 2π ambiguities and providing redundant measurements for improved precision. For directly measured velocities, the uncertainty is better than 1% and for transit time measurements the uncertainty is on the order of 1-2%.

Knowing the initial densities of the MgO and the flyer plate and measuring the V_F and the MgO U_S, we calculate the MgO Hugoniot state density (ρ), pressure (P), and particle velocity (U_P). The Hugoniot state is determined using a Monte Carlo impedance matching analysis [12] to solve the Rankine-Hugoniot (RH) equations [37]. The Monte Carlo method accounts for the uncertainties in the experimental measurement and the Al and Cu Hugoniot standards. The experimental data are listed in the supplement [36].

Figure 2 plots the experimental and DFT principal Hugoniot in ρ-P space. The Z experimental data span the range from 0.27 TPa up to 1.2 TPa - the highest, directly measured Hugoniot states attained in MgO. Also included are the DFT simulation results for the B1, B2, and liquid phases of MgO (discussed later). Although the VISAR diagnostic does not give direct information about the MgO phase upon shock compression, we can infer phase transitions given our data. Figure 2 shows an extrapolation of the linear fit to the $U_S - U_P$ data for B1-phase Hugoniot states < 230 GPa (converted to ρ-P using the RH equations) determined from the previous experiments [21–25]. Below $\approx$ 360 GPa, the Z experimental data are consistent with the gas-gun data but above 360 GPa they deviate from the extrapolation. This suggests that the B1 phase is stable up to 360 GPa and likely undergoes a phase transition from the B1 state to another phase, presumably the B2 state, at that shock pressure. At pressures > 700 GPa we observed reflectivity of the shock front, from which we infer that the MgO has melted into a conductive fluid, similar to what is observed for quartz [9]. These observations suggest the existence at least three phase regions.

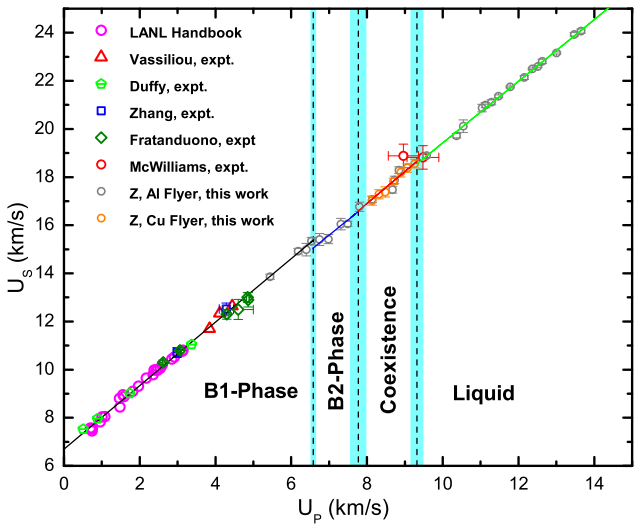

FIG. 3. Experimental $U_S - U_P$ data including results from Refs. [21–25, 32]. The optimized linear fits determined from the MCO method are plotted. The dashed vertical lines indicate the optimized phase boundaries and the shaded cyan regions indicate the uncertainty.

To further investigate the phase region between the B1 and the liquid, we analyze the $U_S - U_P$ data using a Monte Carlo optimization (MCO) method similar to the method used in work on carbon [38]. Slope changes in the $U_S - U_P$ data and changes in reflectivity often indicate phase transitions and phase boundaries. However, between the B1 phase (>360 GPa) and below the liquid phase (<700 GPa) inferring the phase from the $U_S - U_P$ data or the VISAR signals is more difficult because no obvious breaks are observed in the Hugoniot nor do we observe reflectivity.

Using the MCO method, we fit four lines to the experimental $U_S - U_P$ data. While the experimental data do not convincingly distinguish between a three or a four line fit, we chose a four line fit because the phase information from our *ab initio* calculations show four distinct regions along the Hugoniot. In fitting the four lines, the $U_S - U_P$ data were converted to a "cloud" of points, allowing region boundaries to move smoothly during optimization [38]. For a particular set of data clouds, the eleven parameters (four slopes, four intercepts, and three region boundaries) were obtained by minimizing the square minimum distances to each cloud point. Revised clouds were generated by randomly drawing a new center for each cloud. Optimization was repeated ($\approx$ 10000 times) using the revised clouds to characterize the distributions of the parameters. The parameters are listed in the supplement [36]. It is important to note that this analysis is only possible because of the high precision data produced from the steady shocks.

Figure 3 shows the compiled experimental $U_S - U_P$ Hugoniot data, the four linear fits, and the phase regions determined from the MCO method. Following the literature [31] and our DFT results, we propose the four regions be classified as follows: 1. The B1 solid from ambient to 363 GPa; 2. The B2 solid from 363 to 462 GPa; 3. The B2-liquid coexistence region between 462 and 620 GPa; and 4. The liquid state above 620 GPa. However, as our continuum level experiments do not provide microstructure information, we performed *ab initio* calculations of the Hugoniot and the phase diagram to better understand the high pressure states of MgO.

The high precision requirements of this work necessitated refinements of previous *ab initio* methods [29–31]. We performed calculations utilizing DFT and QMC focusing on the solid-solid phase transformation from B1 to B2 and the melting of MgO along the Hugoniot, presumably from the B2 phase. Using DFT to calculate the Hugoniot requires prior knowledge of the phase, so we first calculated the phase diagram. We used a three-part approach to determine the phase boundaries. To determine the melt boundary from both the B1 and B2 phases, we performed two-phase calculations of melting using VASP 5.2.11[39, 40]; further details are presented in the supplemental material [36]. To determine the solid-solid phase boundaries we decomposed the solid's Helmholtz free energy into two pieces.

$$F_{sol}(V,T) = E(V) + F_{vib}(V,T) \tag{1}$$

The first piece is the density dependent energy of either the B1 or B2 phase. This is calculated via diffusion QMC using QMCPACK [41] following methodology detailed in Ref. 42 with particular concern paid to the construction of pseudopotentials. The second piece of the free energy is due to the finite temperature motion of the ions and electrons and is calculated in two parts. First the harmonic part of the free energy is calculated using the finite displacement method as implemented in the PHON code [43]. The quasiharmonic approximation (QHA) is known to break down as temperatures increase and this is particularly true for MgO [44]. For this reason and because the Hugoniot is expected to cross the phase boundary relatively close to the melt line, we have augmented our QHA calculations of free energy with thermodynamic integration (TI). This is performed by using

$$\Delta S = \int_{T_i}^{T_f} \frac{1}{T} \left(\frac{\partial E}{\partial T} \right)_V dT \tag{2}$$

that allows the change in entropy along an isochore to be calculated directly in terms of the internal energy. The energy is calculated using DFT based quantum molecular dynamics (QMD) at points spaced by 250 K along several isochores in the region of the phase transition. Using entropy from the QHA calculation at low temperatures as a reference, we calculate the Gibbs free energy of both phases and determine the phase transition pressure directly. This method also determines the range of validity

TABLE I. Phase boundaries on the principal Hugoniot.

Method	B1-B2 (GPa)	B2-Coexist. (GPa)	Coexist.-Liquid (GPa)
Z Expt. (MCO)	363±6	462±20	620±17
Calc. (this work)	330	475	620
Cebulla, DFT Calc. [31]	350	440	600

for the QHA. We find the range to be smaller than previously estimated[29] with significant deviations in the free energy occurring by 5000 K and 400 GPa. The positive effect of the anharmonic entropy was significantly larger in the B1 phase than in the B2 phase, moving the phase boundary to higher pressures at high temperature. Specific computational details are in the supplement [36].

With the calculated phase boundaries established, we then calculated the Hugoniot states using QMD. Long QMD calculations (100s of fs) at several temperatures for each density and microstructure were performed to determine the average pressure and internal energy. The Hugoniot state for each candidate microstructure was then found by finding the temperature at which the RH energy equation was satisfied. Finally, the pressure and temperature of these shock states were compared to the phase boundaries to determine if they were thermodynamically stable. Additional details of the procedure and comparisons to earlier DFT results [17, 31] are presented in the supplementary material[36]. The resulting P-T phase diagram and Hugoniot states are shown in Fig. 4.

Comparing the data from this approach to experimental Hugoniot data also provides a means to validate the calculations. The calculations and the experiments are in good agreement in $\rho - P$ space (Fig. 2) and in $P - T$ space (Fig. 4). The *ab initio* calculated phase boundaries along the Hugoniot corroborate the MCO fitting method results for the experimental data suggesting the Hugoniot has four major regions: B1, B2, coexistence, and liquid. Table I lists the phase boundaries along the principal Hugoniot from the MCO method and the quantum mechanical simulations. Combining the experimental data from Fig. 2 and the calculations presented in Fig. 4, we find that along the Hugoniot there is an $\approx 5\%$ volume collapse during the solid-solid phase transition and a melting transition that is driven primarily by in increase in entropy rather than a change in density.

Both the experimental and DFT results show a minimum shock pressure of 620 GPa is required to achieve complete melting of MgO initially at ambient temperature. In the giant impact scenario, the proto-Earth is assumed to have an elevated surface temperature prior to the moon-forming event [2]. We have performed additional DFT simulations to calculate the Hugoniot of MgO starting from an initial temperature of 1900 K. From $T_0 = 1900$K, a minimum shock pressure of 445 GPa is required to achieve complete melt in the MgO. Assuming planar normal impact, we can determine a minimum impact velocity required to melt MgO. Table II lists the required impact velocities for impactors of common planetary materials. In a real impact event, oblique impact [47], shock attenuation [48], and that MgO resides in a solid solution with other minerals will affect the impact velocity required for complete melting of the mantle.

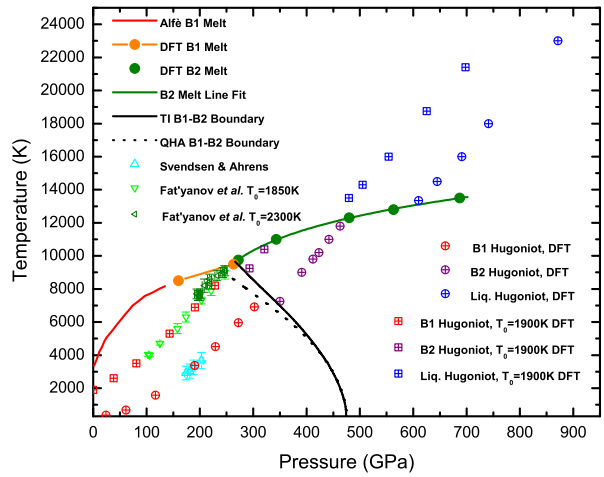

FIG. 4. P-T phase diagram of MgO with calculated Hugoniots starting at ambient and elevated initial temperature conditions. Experimental P-T data [28, 45] and the low pressure B1-B2 melt line from Ref. 46 are included.

TABLE II. Impactor velocities for common planetary materials required to completely melt MgO assuming planar normal impact.

Initial MgO Temp. $[K]$	Impactor $[300K]$	Impact Velocity $[km/s]$
300	MgO	18.6
300	Dunite	19.4
300	Iron	15.3
300	Quartz	20.1
1900	MgO	16.0
1900	Dunite	16.3
1900	Iron	12.9
1900	Quartz	17.7

We have performed an extensive experimental and computational study of the high P–T behavior of MgO up to 1.2 TPa. Contrary to earlier work [32], the data suggests that along the Hugoniot the B1-B2 transition is sharp and driven by volume collapse while the B2-melt transition is gradual and is characterized by a large entropy change. Our results place a lower bound on impact velocities for complete melt in MgO-dominated bodies. The data and phase diagram provide a solid basis for the development of equations of state for the complex minerals relevant for planetary collision and evolution studies.

The authors thank the Z-Operations and Fabrication team for assembling targets and fielding the Z experiments. The authors also thank K. Cochrane and R. Kraus for insightful discussions. We also thank

O. Fat'yanov for sharing his unpublished data. Quantum Monte Carlo calculations by LS were supported through the Predictive Theory and Modeling for Materials and Chemical Science program by the Office of Basic Energy Science (BES), Department of Energy (DOE). Sandia National Laboratories is a multiprogram laboratory managed and operated by Sandia Corporation, a wholly owned subsidiary of Lockheed Martin Corporation, for the U.S. Department of Energy's National Nuclear Security Administration under Contract No. DE-AC04-94AL85000.

* sroot@sandia.gov

[1] W. K. Hartmann and D. R. Davis, Icarus **24**, 504 (1975).
[2] R. M. Canup, Science **338**, 1052 (2012).
[3] M. Cuk and S. T. Stewart, Science **338**, 1047 (2012).
[4] U. Wiechert, A. N. Halliday, D.-C. Lee, G. A. Snyder, L. A. Taylor, and D. Rumble, Science **294**, 345 (2001).
[5] A. Mastrobuono-Battisti, H. B. Perets, and S. N. Raymond, Nature **520**, 212 (2015).
[6] K. Pahlevan and D. J. Stevenson, Earth Planet. Sci. Lett. **262**, 438 (2007).
[7] B. C. Johnson, D. A. Minton, H. J. Melosh, and M. T. Zuber, Nature **517**, 339 (2015).
[8] R. Boehler, Rev. Geophysics **38**, 221 (2000).
[9] M. D. Knudson and M. P. Desjarlais, Phys. Rev. Lett. **103**, 225501 (2009).
[10] R. G. Kraus, S. T. Stewart, D. C. Swift, C. A. Bolme, R. F. Smith, S. Hamel, B. D. Hammel, D. K. Spaulding, D. G. Hicks, J. H. Eggert, and G. W. Collins, J. Geophys. Res. - Planets **117**, E09009 (2012).
[11] D. K. Spaulding, R. S. McWilliams, R. Jeanloz, J. H. Eggert, P. M. Celliers, D. G. Hicks, G. W. Collins, and R. F. Smith, Phys. Rev. Lett. **108**, 065701 (2012).
[12] S. Root, K. R. Cochrane, J. H. Carpenter, and T. R. Mattsson, Phys. Rev. B **87**, 224102 (2013).
[13] W. F. McDonough and S. Sun, Chem. Geology **120**, 223 (1995).
[14] J. S. Kargel, G. Komatsu, V. R. Baker, and R. G. Strom, Icarus **103**, 253 (1993).
[15] G. J. Taylor, Chemie der Erde **73**, 401 (2013).
[16] N. M. Batalha *et al.*, Astrophys. J. **27**, 729 (2011).
[17] N. De Koker and L. Stixrude, Geophys J. Int. **178**, 162 (2009).
[18] A. Zerr and R. Boehler, Nature **371**, 506 (1994).
[19] T. S. Duffy, R. J. Hemley, and H. Mao, Phys. Rev. Lett. **74**, 1371 (1995).
[20] F. Coppari, R. F. Smith, J. H. Eggert, J. Wang, J. R. Rygg, A. Lazicki, J. A. Hawreliak, G. W. Collins, and T. S. Duffy, Nature Geosciences **6**, 926 (2013).
[21] S. P. Marsh, *LASL Shock Hugoniot Data*, Vol. 5 (Univ of California Press, 1980).
[22] M. S. Vassiliou and T. J. Ahrens, Geophys. Res. Lett. **8**, 729 (1981).
[23] T. S. Duffy and T. J. Ahrens, AIP Conference Proceedings **309**, 1107 (1994).
[24] L. Zhang, Z. Gong, and Y. Fei, J. Phys. Chem. Solids **69**, 2344 (2008).
[25] D. E. Fratanduono, J. H. Eggert, M. C. Akin, R. Chau, and N. C. Holmes, J. Appl. Phys. **114**, 043518 (2013).
[26] L. V. Al'tshuler, R. F. Trunin, and G. V. Simakov, Fizika zemli **10**, 1 (1965).
[27] T. S. Duffy and T. J. Ahrens, J. Geophys. Res. **100**, 529 (1995).
[28] O. V. Fat'yanov and P. D. Asimow, in *J. Phys.: Conf. Ser.*, Vol. 500 (IOP Publishing, 2013) p. 062003, and *private communication* O. Fat'yanov, 2015.
[29] A. B. Belonoshko, S. Arapan, R. Martonak, and A. Rosengren, Phys. Rev. B **81**, 054110 (2010).
[30] B. Boates and S. A. Bonev, Phys. Rev. Lett. **110**, 135504 (2013).
[31] D. Cebulla and R. Redmer, Phys. Rev. B **89**, 134107 (2014).
[32] R. S. McWilliams, D. K. Spaulding, J. H. Eggert, P. M. Celliers, D. G. Hicks, R. F. Smith, G. W. Collins, and R. Jeanloz, Science **338**, 1330 (2012).
[33] M. E. Savage *et al.*, in *2007 IEEE Pulsed Power Conference*, Vol. 1-4 (2007) p. 979.
[34] R. W. Lemke, M. D. Knudson, D. E. Bliss, K. Cochrane, J.-P. Davis, A. A. Giunta, H. C. Harjes, and S. A. Slutz, J. Appl. Phys. **98**, 073530 (2005).
[35] S. Root, T. A. Haill, J. M. D. Lane, A. P. Thompson, G. S. Grest, D. G. Schroen, and T. R. Mattsson, J. Appl. Phys. **114**, 103502 (2013).
[36] See Supplemental Material at [URL], which includes references 49–64.
[37] Y. B. Zel'Dovich and Y. P. Raizer, *Physics of Shock Waves and High Temperature Phenomena* (Dover Publications, Inc., Mineola, NY, 2002).
[38] M. D. Knudson, M. P. Desjarlais, and D. H. Dolan, Science **322**, 1822 (2008).
[39] G. Kresse and J. Hafner, Phys. Rev. B **47**, R558 (1993), Phys. Rev. B **49**, 14251 (1994); G. Kresse and J. Furthmüller, Phys. Rev. B **54**, 11169 (1996).
[40] P. E. Blöchl, Phys. Rev. B **50**, 17953 (1994); G. Kresse and D. Joubert, Phys. Rev. B **59**, 1758 (1999).
[41] J. Kim, K. P. Esler, J. McMinis, M. A. Morales, B. K. Clark, L. Shulenburger, and D. M. Ceperley, J. Phys. Conf. Series **402**, 012008 (2012).
[42] L. Shulenburger and T. R. Mattsson, Phys. Rev. B **88**, 245117 (2013).
[43] D. Alfè, Computer Physics Communications **180**, 2622 (2009).
[44] Z. Wu, Phys. Rev. B **81**, 172301 (2010).
[45] B. Svendsen and T. J. Ahrens, Geophys. J. R. Astr. Soc. **91**, 667 (1987).
[46] D. Alfe, Phys. Rev. Lett. **94**, 235701 (2005).
[47] R. G. Kraus, S. Root, R. W. Lemke, S. T. Stewart, S. B. Jacobsen, and T. R. Mattsson, Nature Geoscience **8**, 269 (2014).
[48] S. K. Croft, Geol. Soc. America, Spec. Pubs. **190**, 143 (1982).
[49] A. E. Mattsson, P. A. Schultz, M. P. Desjarlais, T. R. Mattsson, and K. Leung, Modelling Simul. Mater. Sci. Eng. **13**, R1 (2005).
[50] R. Armiento and A. E. Mattsson, Phys. Rev. B **72**, 085108 (2005).
[51] A. E. Mattsson, R. Armiento, J. Paier, G. Kresse, J. M. Wills, and T. R. Mattsson, J. Chem. Phys. **128**, 084714 (2008).
[52] N. D. Mermin, Phys. Rev. **137**, A1441 (1965).
[53] T. R. Mattsson and R. J. Magyar, in *Shock Compression of Condensed Matter – 2009*, AIP Conf. Proc., Vol. 1195,

edited by M. L. Elert *et al.* (AIP, Melville, New York, 2009) pp. 797–800.
[54] D. Alfe, M. Alfredsson, J. Brodholt, M. Gillan, M. Towler, and R. Needs, Phys. Rev. B **72**, 014114 (2005).
[55] W. Chaibi, R. J. Pelez, C. Blondel, C. Drag, and C. Delsart, Eur. Phys. J. D **58**, 29 (2010).
[56] T. Andersen, Phys. Reports **394**, 157 (2004).
[57] S. Speziale, C.-S. Zha, T. S. Duffy, R. J. Hemley, and H.-k. Mao, J. Geophys. Res.-Solid **106**, 515 (2001).
[58] Y. Fei, Am. Mineral. **84**, 272 (1999).
[59] L. Operti, E. C. Tews, T. J. MacMahon, and B. S. Freiser, J. Am. Chem. Soc. **111**, 9152 (1989).
[60] K. Huber and G. Herzberg, *Molecular Spectra and Molecular Structure 4. Constants of Diatomic Molecules* (van Nostrand, Princeton, 1979).
[61] D. R. Lide, ed., *CRC Handbook of Chemistry and Physics*, 84th ed. (CRC Press, Boca Raton, Florida, 2003).
[62] K. K. Irikura, J. Phys. Chem. Ref. Data **36**, 389 (2007).
[63] M. A. Morales, J. McMinis, B. K. Clark, J. Kim, and G. E. Scuseria, J. Chem. Theory Comp. **8**, 2181 (2012).
[64] P. Vinet, J. Ferrante, J. R. Smith, and J. H. Rose, J. Phys. C: Solid State **19**, L467 (1986).